Exposure Stability of Quantitative Fluorine-18 Measurements On The Biograph Vision Quadra PET/CT System

George Amadeus Prenosil (george.prenosil@insel.ch)
Department of Nuclear Medicine, Inselspital, Bern University Hospital and University of Bern
https://orcid.org/0000-0001-6673-5374
Michael Hentschel
Department of Nuclear Medicine, Inselpsital Bern, Bern University Hospital and University of Bern
Thilo Weitzel
Department of Nuclear Medicine, Inselspital Bern, Bern University Hospital and University of Bern
Hasan Sari
Department of Nuclear Medicine, Inselspital Bern, Bern University Hospital and University of Bern
Kuangyu Shi
Department of Nuclear Medicine, Inselspital Bern, Bern University Hospital and University of Bern
Axel Rominger
Department of Nuclear Medicine, Inselspital Bern, Bern University Hospitla and University of Bern

Original research

Keywords: EARL, exposure, image reconstruction, long axial field of view, quantitative 18F PET/CT

Posted Date: September 15th, 2021

DOI: https://doi.org/10.21203/rs.3.rs-864693/v1

Exposure stability of quantitative fluorine-18 measurements on the Biograph Vision Quadra PET/CT system

George A. Prenosil[1], Michael Hentschel[1], Thilo Weitzel[1], Hasan Sari[1,2], Kuangyu Shi[1,] Axel Rominger[1]

1 Department of Nuclear Medicine, Inselspital Bern, Bern University Hospital, University of Bern, Bern, Switzerland

2 Advanced Clinical Imaging Technology, Siemens Healthcare AG, Lausanne, Switzerland;

** Corresponding Address: George A. Prenosil, Department of Nuclear Medicine, Inselspital Bern, 3010 Bern, Switzerland; Tel.: +41 31 632 76 51, Fax.: +41 31 632 76 63, e-mail: george.prenosil@insel.ch*

1. Abstract

Background: Our aim was to determine sets of reconstruction parameters for the Biograph Vision Quadra (Siemens Healthineers) PET/CT system that result in quantitative images compliant with the European Association of Nuclear Medicine Research Ltd. (EARL) criteria. Using the Biograph Vision 600 (Siemens Healthineers) PET/CT technology but extending the axial field of view to 106 cm, gives the Vision Quadra currently an around fivefold higher sensitivity over the Vision 600 with otherwise comparable spatial resolution. Therefore, we also investigated how the number of incident positron decays - i.e. exposure - affects EARL compliance. This will allow estimating a minimal acquisition time or a minimal applied dose in clinical scans while retaining data comparability.

Methods: We measured activity recovery curves on a NEMA IEC body phantom filled with an aqueous ^{18}F solution and a sphere to background ratio of 10 to 1 according to the latest EARL guidelines. Reconstructing 3570 images with varying OSEM PSF iterations, post-reconstruction Gaussian filter full width at half maximum (FWHM), and varying exposure from 0.2 MDecays/ml (= 10 sec frame duration) to 59.2 MDecays/ml (= 1), allowed us to determine sets of parameters to achieve compliance with the current EARL 1 and EARL 2 standards. Recovery coefficients (RCs) were calculated for the metrics RC_{max}, RC_{mean}, and RC_{peak}, and the respective recovery curves were analysed for monotonicity.

Results: Using 6 iterations, 5 subsets and 7.8 mm Gauss filtering resulted in best EARL-1 compliance and recovery curve monotonicity in all analysed frames. Most robust EARL2 compliance and monotonicity was achieved with 4 iterations, 5 subsets, and 4.6 mm Gauss FWHM in frames with durations between 10 min and 30 sec. RC_{peak} only impeded EARL2 compliance in the 10 sec frame.

Conclusions: While EARL1 compliance proved to be robust over all exposure ranges, EARL2 compliance required exposures between 0.6 MDecays/ml to 11.5 MDecays/ml. The Biograph Vision Quadra's high sensitivity makes frames as short as 10 sec feasible for comparable quantitative images. Lowering EARL2 RC_{max} limits closer to unity would possibly even permit 10 sec EARL2 compliant frames.

Key Words: EARL, exposure, image reconstruction, long axial field of view, quantitative ^{18}F PET/CT

2. Background

Clinical positron emission tomography (PET) systems have found a widespread use in many fields of diagnostics and follow up care. This success is at least partially owed to the technological progress PET has experienced since its debut roughly 45 years ago [1]. In combination with computed tomography (CT), PET/CT became an ever-evolving instrument for quantitatively measuring the spatial distribution of positron emitting tracers. Continuous improvement in detector technology, such as employing small and fast lutetium oxyorthosilicate (LSO) crystals for photon conversion and fast electronics increased spatial resolution and sensitivity of molecular imaging. Additionally, time-of-flight (TOF) technology increased sensitivity and signal to noise ratio (SNR) [2-4]. Recent development in detector technology include the replacement of analogue photomultiplier tubes with digital silicon photomultipliers, giving rise to so-called digital PET/CT systems. Their higher gain, better coverage of the LSO crystals, better energy resolution and faster read-out made digital PET/CT systems generally outperform their analogue forerunners in lesion detection and acquisition duration [5-7]. On the software side, modern non-linear reconstruction algorithms use resolution recovery techniques for

reducing the partial volume effect (PVE) [8, 9]. The PVE, inherent to all imaging devices, blurs the image and impedes tracer uptake quantification in small objects.

Current state of the art are digital total-body PET/CT systems with a long axial field of view (AFOV) such as the Biograph Vision Quadra (Siemens Healthineers) and the uEXPLORER (United Imaging) [10]. The Biograph Vision Quadra essentially is comprised of an axial concatenation of the equivalent of four Biograph Vision 600 scanners [11], providing an AFOV of 106 cm. Besides enabling the simultaneous imaging of distant anatomical regions, the long AFOV increases count rate and thus sensitivity. The Quadra's current clinical high sensitivity mode, where not all lines of response are used to form the PET image, increases sensitivity by a factor of five when compared to the preceding Biograph Vision 600 [12, 13]. A future upgrade to an ultra-high sensitivity mode, with all lines of response used, will raise sensitivity even further. This sensitivity increase allows either a reduction in patient radiation dose or shortening the acquisition duration. The latter aspect makes the Biograph Vision Quadra an ideal imaging tool in dynamic total-body studies with high spatial resolution.

However, differences in instrumentation and image reconstruction between the commercially available PET/CT systems impacts image comparability. Hence, data acquired on differing PET/CT systems add statistical spread to multicenter clinical studies [14, 15], which in its turn renders quantitative tracer uptake measurements a poorer diagnostic indicator [16]. Therefore, efforts for establishing PET/CT comparability have been undertaken. Since 1994, National Electrical Manufacturers Association (NEMA) performance measurements evaluate comparatively PET/CT systems with standardized procedures [17], providing data on a PET system's imaging characteristics. The NEMA NU 2 standards publications are updated regularly, mirroring the technological progress in the field [18]. Even though the NEMA standards provide various metrics for quantifying and comparing PET/CT performance, differences in image formation remained to be addressed. Therefore, the method of transconvolution has been introduced that recasts images acquired on different PET/CT systems as if they had all been acquired on the same PET system [19] or with the same positron emitter [20, 21]. Another approach uses adapted post reconstruction filtering for data harmonization [22]. Finally, the

European Association of Nuclear Medicine Research Ltd. (EARL) initiative introduced complete harmonizing strategies [23, 24] in their accreditation program. EARL accreditation is meant especially for participating in multicenter clinical studies [25], where it guarantees comparable data sets even between different generations of PET/CT systems or different manufacturers [26].

Although NEMA performance measurements result in various metrics for comparing imaging properties and sensitivity between different PET/CT systems [18], optimal clinical acquisition durations are not specifically addressed in NEMA image quality measurements nor in the EARL guidelines [23, 24]. EARL guidelines demand clinically relevant acquisition durations of five minutes per bed position, but make no considerations to a PET/CT system's sensitivity. Work by Kaalep *et al* [27] describes the effect of long and short acquisitions on PET data harmonization using the EARL standards, but no official EARL recommendation for image exposure resulted thereof. As shown for the Biograph Vision 600 [7], knowledge of the required minimal exposure on a given PET/CT system is important for estimating the shortest feasible acquisition duration or the minimum injected dose, while simultaneously retaining reproducible and comparable PET/CT images. Pilz *et al.* [28] demonstrated a certain tolerance of EARL compliant FDG PET/CT measurements to image noise, reducing clinical acquisition duration down to 57 sec per bed position on their 3D TOF Ingenuity TF PET/CT system (Philips, Cleveland, OH). With image reconstruction parameters optimized for low exposures, even shorter EARL compliant acquisition durations can be possible.

We have previously defined exposure in PET/CT as the number of incident counts to demonstrate its impact on metrics for textural features in PET images [29]. Here, we explore how exposure affects EARL compliance on a PET/CT system with a long AFOV. This question is especially relevant for dynamic studies, where tracer uptake changes during acquisition, and potentially degrades comparability of measurement points within a time activity curve.

From activity recovery measurements, we deduced image reconstruction parameter sets that resulted in EARL compliance [24, 25] under varying exposure for the Biograph Vision Quadra. This allowed us to formulate minimal and maximal exposure regimes for this new PET/CT system.

Reflecting advances in PET instrumentation such as increased spatial resolution, TOF, and point-spread function (PSF) image reconstructions, two EARL standards - EARL1 and EARL2 - are currently in effect [27, 30, 31]; we thus addressed both. Furthermore, monotonicity of recovery curves was analyzed.

3. Material and Methods

The aim of this study was to identify a complete image parameter space for obtaining quantitative, EARL compliant PET/CT images for the Biograph Vision Quadra. For this purpose, the examined parameters were the number of reconstruction iterations, post-reconstruction Gaussian filter full width at half maximum (FWHM), and exposure. All measurements were performed on a PET phantom.

3.A. Phantom measurements

A NEMA IEC body phantom [18, 32] with six hollow spheres of 10, 13, 17, 22, 28, and 37 mm internal diameter was filled with an aqueous solution of [^{18}F]FDG to a sphere to background activity concentration ratio of 10 to 1. At the start of PET acquisition, the background activity concentration was 1.97 kBq/ml; the respective foreground activity concentration was 19.7 kBq/ml. The six spheres were positioned at a radius of 57.2 mm around the phantom center, surrounding a cold lung insert of 50 mm diameter filled with polystyrene beads. The phantom was placed with the spheres in the center of the field of view and perpendicular to the axial plane as required by the NEMA NU 2-2018 protocol [18].

List mode data was acquired on the Biograph Vision Quadra lasting for one hour for one bed position. Using this data, images were reconstructed using a software prototype for image reconstruction (Siemens Healthineers) using the PSF+TOF (TrueX) algorithm. Multiple images were reconstructed using frame durations of 10 sec, 30 sec, 60 sec, 180 sec, 300 sec, and 600 sec. The one-hour long image reconstruction served as a best, low noise acquisition against which all other reconstructions were compared. Five minutes frame duration is the current EARL specification recommended for clinical images [24]. The different acquisition durations resulted in exposures of 0.2, 0.6, 1.2, 3.5, 5.8, 11.5, and

59.2, all values given in units of MDecays/ml. All images were reconstructed into a 440 x 440 matrix, with 1.65 mm slice thickness for an isometric voxel spacing. In 510 reconstructions per frame duration, we then systematically varied the Gaussian post-reconstruction filter FWHM from 0 mm (all pass) to 10 mm in increments of 0.2 mm and the number of reconstruction iterations from one to ten in increments of one to identify the particular parameter set that resulted in EARL1 and EARL2 compliance for a given exposure. The number of iterative subsets was kept constant at five. All image reconstructions were performed offline on a HP Z8 G4 workstation (HP Inc., Palo Alto, CA, USA), equipped with a 3.1 GHz Intel® Xeon® Gold 6254 CPU, and running the scriptable software prototype dedicated to image reconstruction.

The PET data were corrected for scatter, randoms, decay and attenuation. The CT scans for attenuation correction were acquired with 120 keV tube voltage, 80 mAs tube current and with 0.8 pitch. The CT image was reconstructed into a 512 x 512 matrix, with a 5 mm slice distance, and with an axial increment of 1.65 mm for isometric PET voxels.

3.B. Definitions

3.B.1. Exposure

Exposure E was defined as the total number of expected decay events per volume during acquisition time Δt, and starting with a mean initial activity concentration A_0. When using a short-lived isotope, such as ^{18}F, exposure must be calculated as the integral over all decays encountered, instead as just the product of activity concentration and acquisition duration [29]:

$$E = \int_0^{\Delta t} A_0 * 2^{-\frac{t}{t_{1/2}}}\, dt \quad (1)$$

The integral resolves into

$$E = \frac{A_0}{\ln 2} * \left(t_{1/2} - t_{\frac{1}{2}} * 2^{-\frac{\Delta t}{t_{1/2}}} \right) \quad (2)$$

Here, $t_{1/2}$ is 109.77 min, the half-life of ^{18}F. Exposure was always defined for the foreground activity concentration at acquisition start, i.e. A_0 in the phantom spheres. In clinical images, exposure would thus normally be calculated for the investigated lesions and not for the background signal.

3.B.2. Quantitative Image Metrics

In this work, phantom PET/CT images were analyzed for the recovery coefficients (RC) RC_{max}, RC_{peak}, and RC_{mean} according to the current EARL guidelines [24, 25]. The RC_{max} metric was the value of the hottest voxel found within the phantom sphere location, with RC_{peak} comprising the mean value within a 1ml sphere around that voxel. The RC_{mean} metric was calculated from the average value in an automatically grown volume of interest (VOI) around the RC_{max} location, which only included voxels with a value equal or greater than 50 % of the maximal value found in said VOI (VOI A_{50}) [33, 34]. All RCs were normalized to the 19.74 kBq/ml ^{18}F found in the spheres at the start of the PET acquisition to obtain recovery coefficients.

To achieve EARL compliance, recovery coefficients for RC_{max}, RC_{peak}, and RC_{mean} had to be within the limits for all phantom spheres published in the EARL guidelines for ^{18}F PET/CT on July 2020 [31]. Table I shows the currently valid EARL1 and EALR2 limits.

Table I: EARL1 and EARL2 limits. *At the time of this work, RC_{max} for total body scanner was under investigation. ** RC_{peak} limits were under revision. Table adapted from the EARL webpage [31].

NEMA IEC phantom spheres			**^{18}F standard 1 RC limits**		**^{18}F standard 2 RC limits**		
Sphere *i*	Diameter (mm)	Volume (mL)	RC_{max}	RC_{mean}	RC_{max}*	RC_{mean}	RC_{peak}**
1	37	26.52	0.95 – 1.16	0.76 – 0.89	1.05 – 1.29	0.85 – 1.00	0.90 – 1.10
2	28	11.49	0.91 – 1.13	0.72 – 0.85	1.01 – 1.26	0.82 – 0.97	0.90 – 1.10
3	22	5.57	0.83 – 1.09	0.63 – 0.78	1.01 – 1.32	0.80 – 0.99	0.90 – 1.10
4	17	2.57	0.73 – 1.01	0.57 – 0.73	1.00 – 1.38	0.76 – 0.97	0.75 – 0.99
5	13	1.15	0.59 – 0.85	0.44 – 0.60	0.85 – 1.22	0.63 – 0.86	0.45 – 0.70
6	10	0.52	0.34 – 0.57	0.27 – 0.43	0.52 – 0.88	0.39 – 0.61	0.27 – 0.41

The metrics RC_{max}, RC_{peak} and RC_{mean} from phantom data for every sphere *i* was then plotted against sphere diameter to obtain recovery curves.

3.C. Data analysis

3.C.1. EARL compliance analysis of recovery curves

We introduced the normalized root mean square error (nRMSE) to assess quantitatively EARL compliance of recovery curves. The nRMSE incorporated the distance d_i of a recovery curve value RC_i to the mean EARL compliance value RC_{mean} as residuals for every sphere i. RC_{mean} value arose from the average of the low and high EARL limits for a given recovery metric at position i in the RC. To arrive at a comparable measure of compliance, regardless of the recovery metric used, d_i was normalized to the relative width of the EARL limits band for sphere i.

$$d_i = \frac{RC_i - RC_{mean}}{(EARL_{high,i} - EARL_{low,i})}, \text{ and } RC_{mean} = \frac{(EARL_{high,i} - EARL_{low,i})}{2} \quad (3)$$

From d_i, nRMSE was calculated:

$$nRMSE = \sqrt{\frac{1}{i}\sum d_i^2} \quad (4)$$

For a concise compliancy report, the nRMSE values for the recovery metrics RC_{max} and RC_{mean} were aggregated into a single value according to the formula below:

$$nRMSE = \sqrt{(nMRSE_{SUVmax}^2 + nMRSE_{SUVmean}^2)/2} \quad (5)$$

Because at the time of this work, RC_{peak} was under revision for EARL2, we analyzed this metric separately for EARL2 compliancy, without aggregating it with the other two recovery values. This allowed determining the exact combination of optimal image reconstruction parameters for EARL2 compliant RC_{peak} values.

3.C.2.Statistical data analysis

The Spearman's rank correlation coefficient ρ was used as a metric for monotonicity of recovery curves (RC vs. sphere diameter), with

$$\rho \in \mathbb{R} \mid -1 \leq \rho \leq 1 \quad (6)$$

A ρ = -1 or ρ = 1 indicates perfect decreasing or increasing monotonicity, whereas $\rho = 0$ means complete absence of monotonicity. Recovery curve monotonicity was not an EARL criterion but was added here as a quality metric for recovery curves.

3.C.3.Software

Phantom was analyzed using an in-house software which itself was realized on our rapid application development framework written in Java and Prolog. This software used scriptable batch processing for the automated analysis of 3570 image reconstructions obtained by varying iterations, Gauss FWHM and exposure. The software ran on a HP Z640 workstation (HP Inc., Palo Alto, CA, USA).

4. Results and Discussion

4.A. EARL Compliance testing

Plotting in Figure 1 the reconstruction parameter space as a function of total nRMSE in green for sets that passed and in red for sets that failed EARL1 compliance, revealed the optimal reconstruction parameter combinations for EARL1 compliant PET/CT images for different exposures.

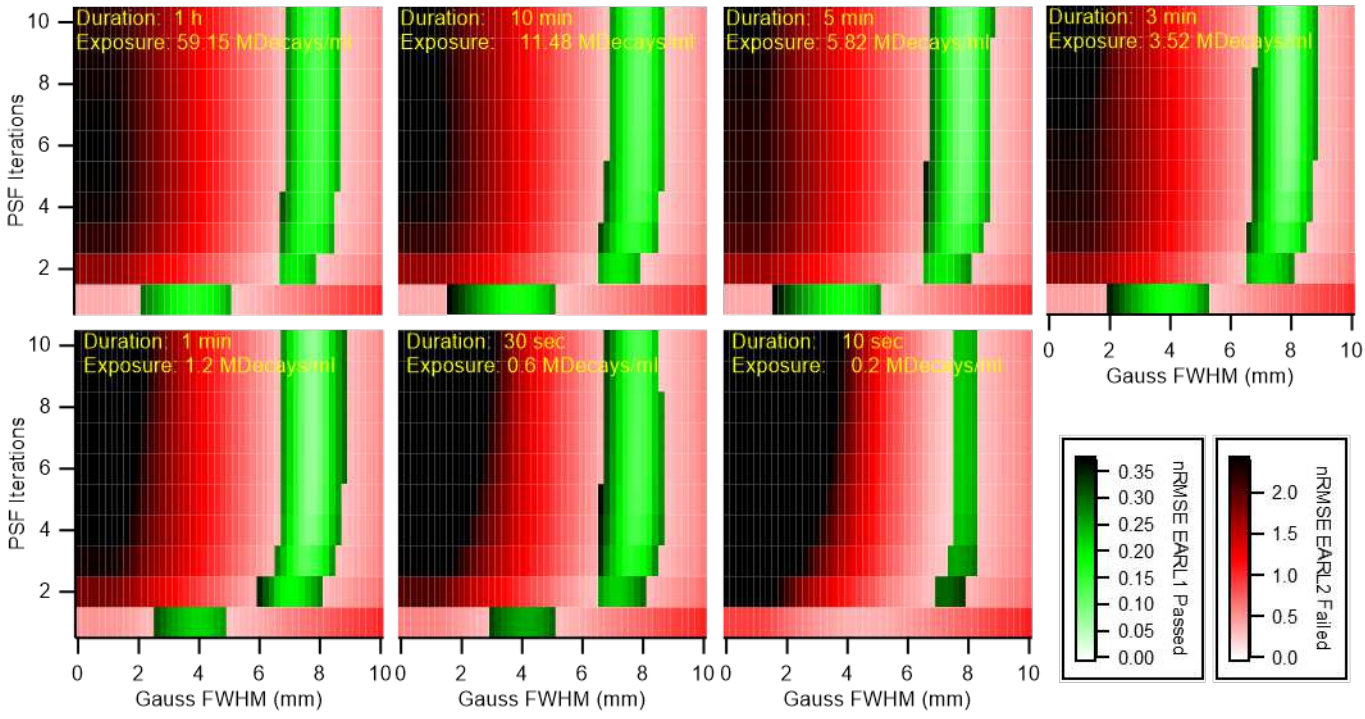

Figure 1: Normalized RMSE for RC_{max} and RC_{mean} in reconstruction parameter space showing EARL1 compliance for all phantom measurements. Green = passed current EARL1 limits; red = failed current EARL1 limits. Each panel represents a decreasing exposure.

The Biograph Vision Quadra achieved exposure stable EARL1 compliance within a Gauss FWHM corridor ranging from 6.8 mm to 8.6 mm and for two to ten iterations in most frames (Green bands in Figure 1). In the 10 sec frame, the accepted Gauss FWHM corridor narrowed down to between 7.6 mm

and 8.2 mm. The lowest nRMSE relative to the EARL1 limits in the 10 sec images was found at 7 iterations, 5 subsets and 7.8 mm Gauss filtering resulted in the lowest nRMSE relative to the EARL1 limits and produced a value of 0.22. The overall lowest nRMSE value of 0.075 was found in the 1 min frame for 6 iterations, 5 subsets and 7.8 mm Gaussian FWHM, suggesting these being the most optimal and stable image reconstruction parameters for EARL1 compliance.

Figure 2 shows the recovery curves resulting from the optimal image reconstruction parameters for all analyzed frames in relation to the respective EARL1 limits. It was usually the largest sphere that would express the highest image noise under low exposure regimes, with RC_{max} values above the specified limits (Figure 2a).

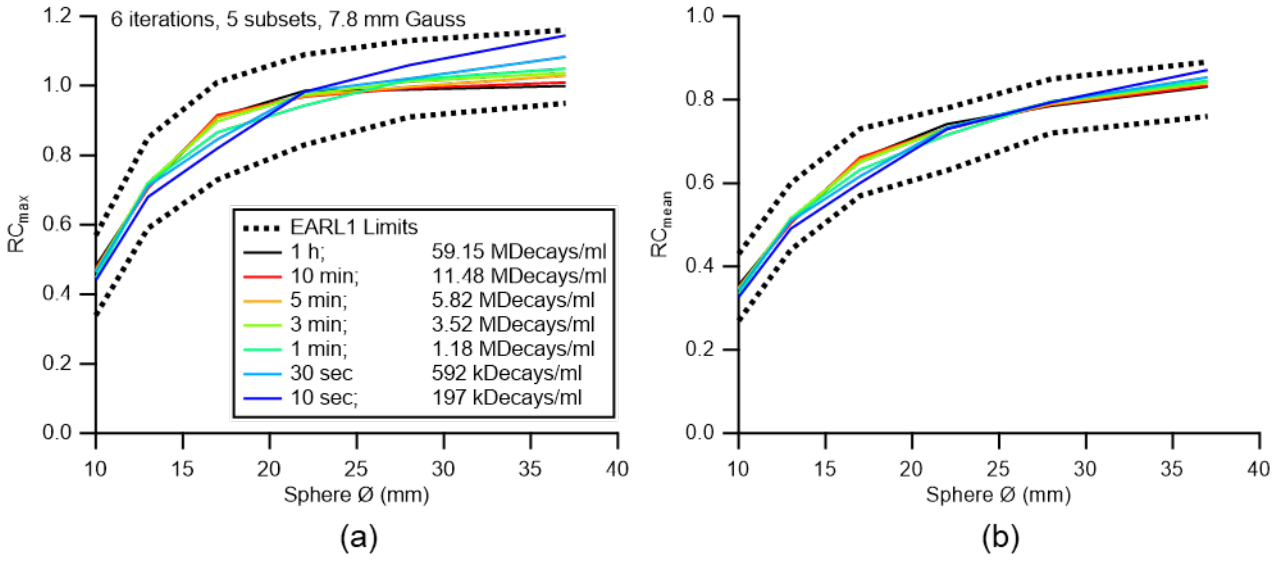

Figure 2: EARL1 compliant RC_{max} (a) and RC_{mean} (b) recovery curves for different exposures resulting from 6 iterations, 5 subsets, and 7.8 mm Gauss FWHM

When analyzing the same image reconstructions for EARL2 compliance, it became clear that RCs from frames below 30 sec and above 10 min were outside the specified EARL limits from Table I. This translated to a minimal exposure of 0.6 MDecays/ml and to a maximal exposure of 11.5 MDecays/ml for EARL2 compliance. Figure 3 shows the total nRMSE for RC_{max} and RC_{mean} as a function of the number of iterations and Gauss FWHM concerning the EARL2 standards. The most stable image reconstructions regarding exposure were achieved with 3 iterations, 5 subsets, and a 4.4 mm Gauss

FWHM. This reconstruction parameter combination resulted in a minimal nRMSE of 0.215 in the 1 min frame. However, the resultant recovery curves showed an increasing non-monotonicity in frames with longer exposures.

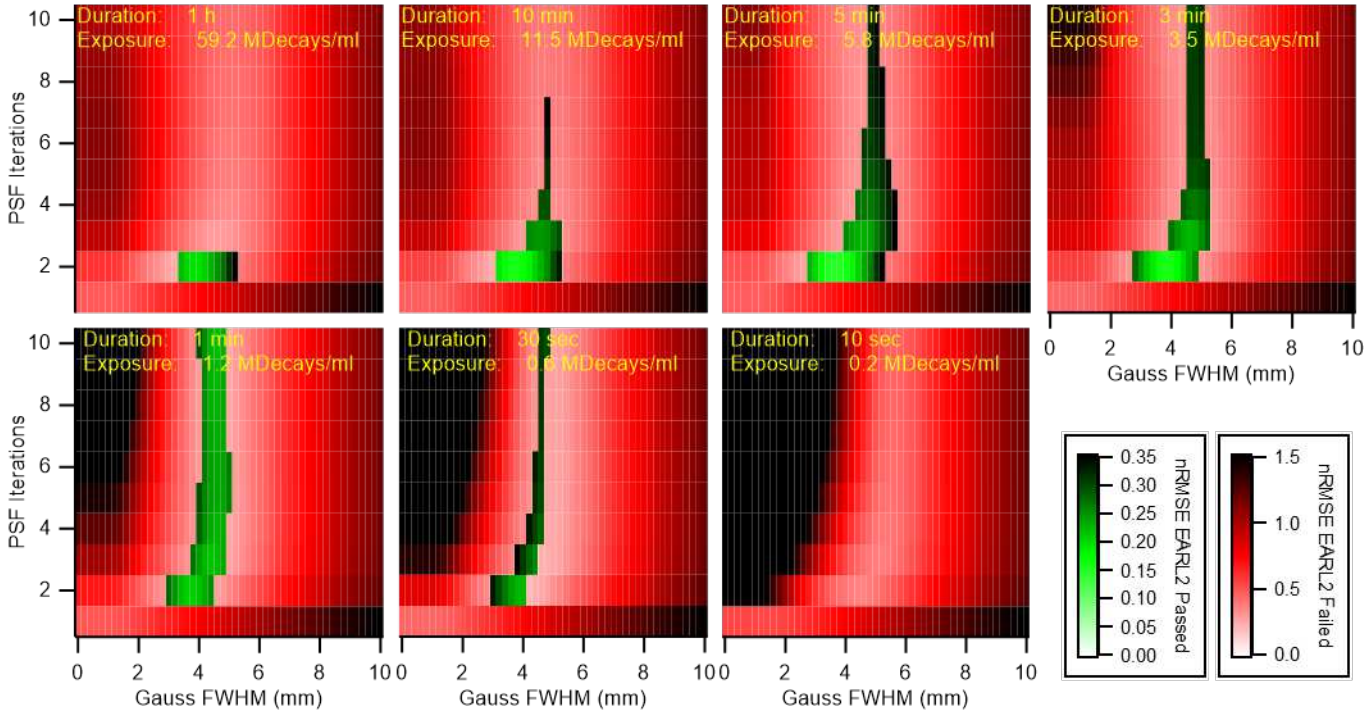

Figure 3: Normalized RMSE for RC_{max} and RC_{mean} in reconstruction parameter space showing EARL2 compliance for all phantom measurements. Green = passed current EARL2 limits; red = failed current EARL2 limits.

When additionally analyzing RC_{peak} for EARL 2 compliance, it could be shown that this metric was always within EARL2 limits for a broad range of reconstruction parameters (Figure 4). Only in the shortest frame was compliance restricted to a Gaussian FWHM of around 5.6 mm. Similar to the other metrics, RC_{peak} was never within EARL2 limits for images reconstructed with only one iteration, and a minimum of three iterations was needed in the 10 sec image. We conclude that for three or more iterations the compliance relevant metrics were RC_{max} and RC_{mean}.

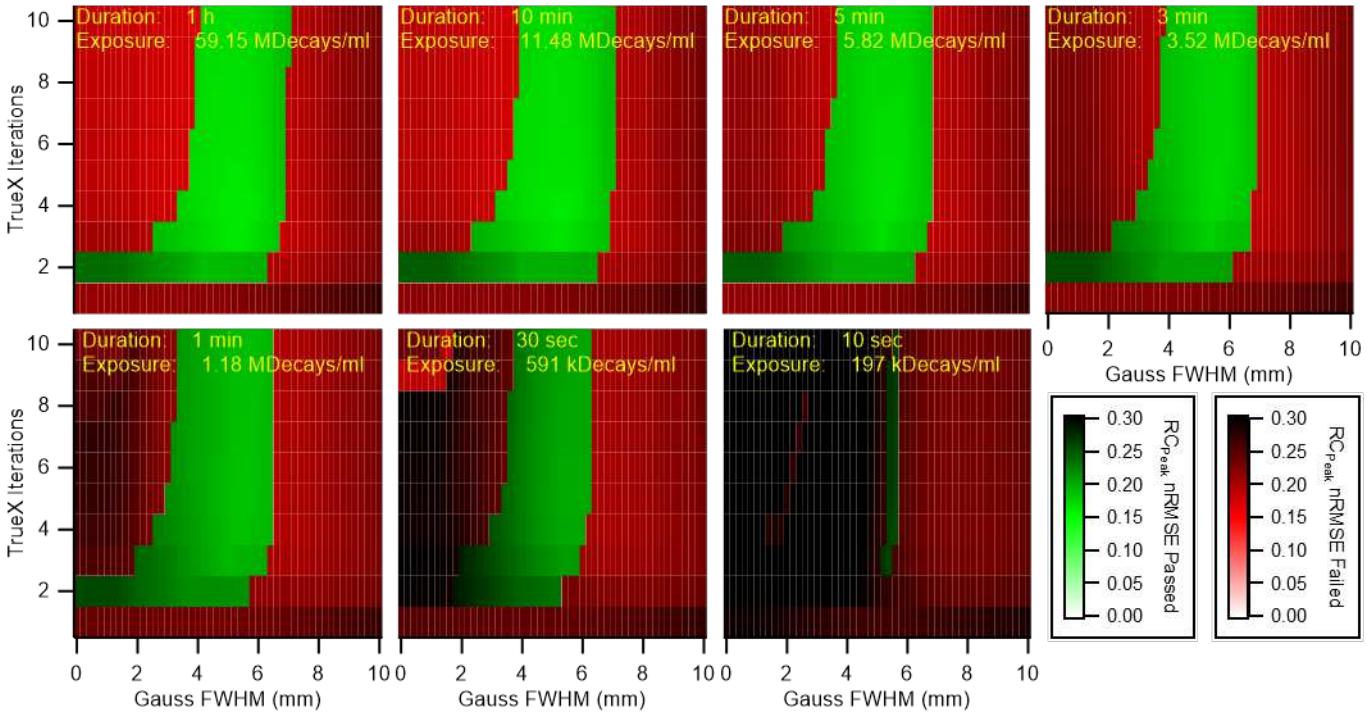

Figure 4: Normalized RMSE for RC_{peak} in reconstruction parameter space. Green = passed current EARL2 limits, red = failed current EARL2 limits.

4.B. Recovery curve monotonicity

Ideally, RCs stay as close as possible to unity, with the unavoidable drop for spheresizes near the Nyquist limit. Furthermore, while ideal recovery curves would be monotonic, real recovery curves recorded on modern PET/CT systems with non-linear reconstruction algorithms are sometimes inflated for certain sphere sizes [35, 36]. Actually, the EARL2 limits intended for newer PET/CT systems even reflect this fact [30]. However, recovery curve non-monotonicity can potentially have clinical implications, e.g. when a therapy-induced shrinkage of a lesion might be actually interpreted as increased tracer uptake. Because RC_{max} was overall the most non-monotonous metric, we analyzed RC_{max} recovery curves for monotonicity. The monotonicity value provided an additional criterion for selecting optimal sets of reconstruction parameters and exposures in Figure 5.

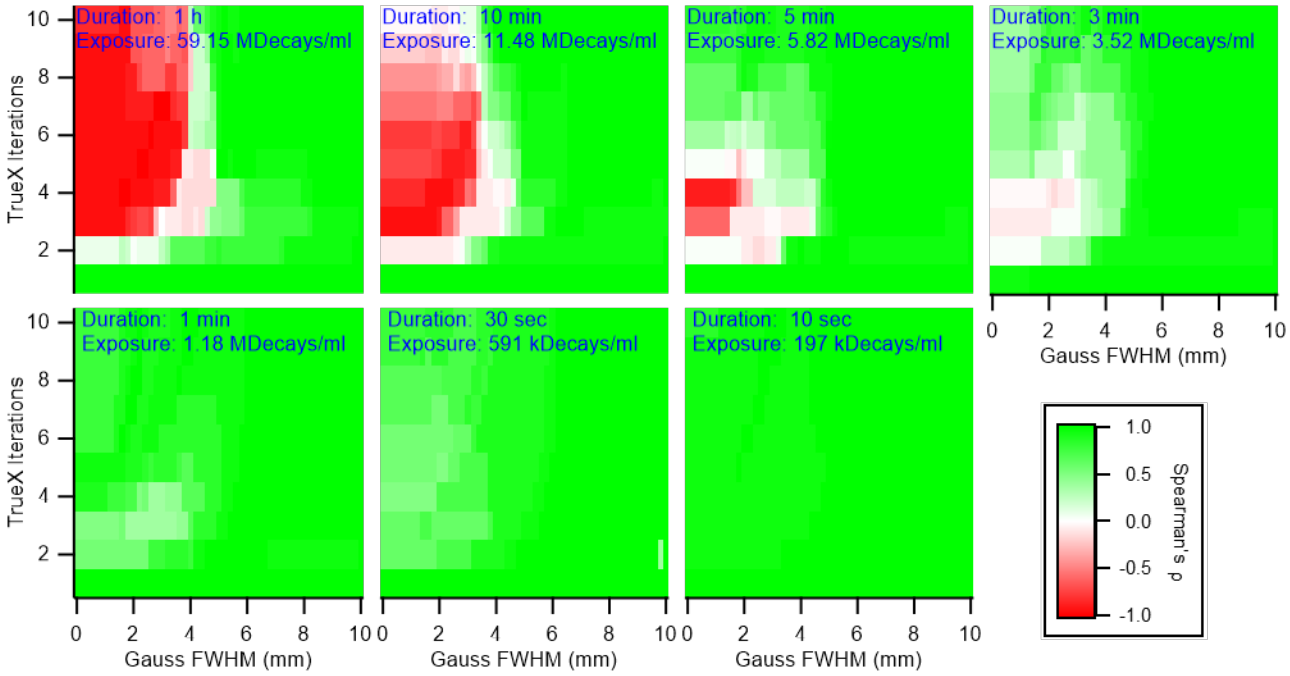

Figure 5: Monotonicity of RC_{max} recovery curves: Shown is the Spearman's ρ as a function of number of TrueX iterations and post-reconstruction Gauss FWHM for different exposures.

While the above-suggested EARL1 compliant image reconstruction parameter sets always resulted in monotonic recovery curves, EARL2 compliant parameters resulted more often in non-monotonic recovery curves ($\rho \approx 0$). From our data in Figures 3, 4, and 5, we therefore recommend a compromise of 4 iterations, 5 subsets and a post-reconstruction Gauss FWHM of 4.6 mm for monotonic EARL2 compliant recovery curves over most exposures. RC_{max} recovery curves from 1 min frames or shorter were generally monotonically rising ($\rho > 0$), as image noise was a function of sphere size. Higher exposures with higher iteration numbers and low post-reconstruction filtering tended to result in monotonically falling RC_{max} curves ($\rho < 0$). Here, the Biograph Vision Quadra over-iterated the smaller spheres, raising RC_{max} values above unity. The PSF reconstruction is essentially a deconvolution algorithm, where de-blurring of objects sized similarly to the system's PSF can lead to overestimation of their activity. This amplification effect increases with the number of iterations [37].

Figure 6 shows the recovery curves resulting from the above-suggested image reconstruction parameters for all analyzed frames together with the respective EARL2 limits. Also shown are recovery curves reconstructed with parameters as suggested previously for the Biograph Vision 600 [7], a

technologically related PET/CT system. These reconstruction parameters resulted in slightly less exposure robust recovery curves, only passing EARL2 compliance between 1 min and 5 min exposure times.

It was apparent, that lowering exposure increased RC_{max} in the largest spheres and decreased RC_{max} in the smallest spheres. The other two metrics, RC_{mean} and RC_{peak}, were more robust in terms of exposure and monotonicity. When EARL2 compliance was not achieved, it was usually RC_{max} in the largest sphere not passing the EARL2 requirements. It is also noteworthy, that in many high exposure reconstructions RC_{max} was close to unity for the two largest spheres, indicating a low-noise image. Nevertheless, this resulted in non-compliance, as EARL2 does not allow an RC_{max} at unity for the three largest spheres (*c.f.* Table I), instead mandating a certain presence of image noise. For example in the failed 4 iterations, 5 subsets, 4.6 mm Gauss FWHM 1 h acquisition in Figure 6, RC_{max} was with 1.04 already below EARL2 limits for the largest sphere. Not having to introduce artificial image degradation to PET/CT systems with a long AFOV certainly warrants a currently ongoing reevaluation of EARL2 limits.

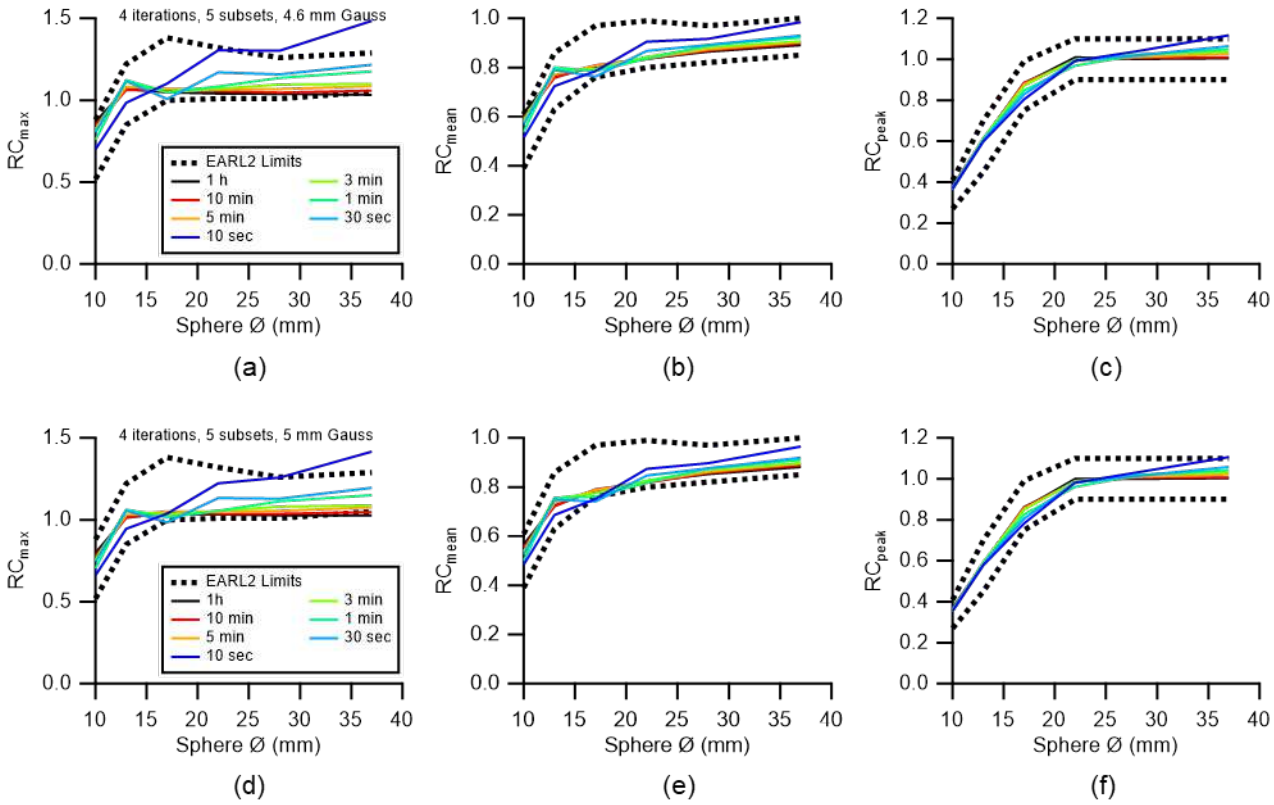

Figure 6: Upper row: Recovery curves calculated from RC_{max} (a) RC_{mean} (b) and RC_{peak} (c) for different exposures resulting from 4 iterations, 5 subsets, and 4.6 mm Gauss FWHM in respect to EARL2 limits. Lower row: Recovery curves calculated from RC_{max} (d) RC_{mean} (e) and RC_{peak} (f) for different exposures resulting from 4 iterations, 5 subsets, and 5 mm Gauss FWHM in respect to EARL2 limits.

The apparent paradoxical behavior of the large objects being more susceptible to image noise is vested in image count statistics: In imaging, the SNR measured within an imaged volume depends on the imaging system's sensitivity s and on number of available incident quanta from activity A, *i.e.* exposure E. This gives the well-known SNR-exposure relationship:

$$SNR \propto \sqrt{s * A * \Delta t} \text{ with } A * \Delta t = E \quad (7)$$

Even though the incident quanta strictly follow a random Poisson process, the intensity distribution that makes up the final PET image depends on the chosen reconstruction method: While for filtered back projection, a Gaussian distribution can be assumed, images reconstructed with OSEM and PSF show lognormal [38, 39] or gamma-distributions [40]. Decreasing exposure broadens intensity distributions, and gives rise to tail-heavy distributions in OSEM and PSF reconstructions [29]. RC_{max}, being the supremum in the intensity probability distribution of the PET image, is therefore expected to rise with decreasing exposure. For the same reasons, object size correlates positively with RC_{max}: The probability for finding higher RC_{max} becomes higher within larger sets of image volume elements. On the other hand, with object size falling below a critical value relative to the system's PSF extent, the lower background noise from the spill-in of background intensity can dominate over object noise. In small objects, the PVE spills some of its noise out into the background, and a lower RC_{max} can therefore be expected in frames of shorter durations. It must be noted, that in PET/CT systems with TOF, the effect of object size on RC_{max} might be somewhat diminished, as relative gains in sensitivity from TOF are proportional to twice the object diameter [2].

Two facts limit the informative value of this work: First, at the time of this study the Biograph Vision Quadra was using a maximum ring distance of 85 (MRD 85), thus using maximally one fourth of the crystal rings for image acquisitions. While this gives the Quadra a homogenous sensitivity over the

entire AFOV [13], a future update using the full ring distance of 322 (MRD 322) will bring forth an increase in sensitivity. Second, at the time of this study, the Biograph Vision Quadra was not equipped with continuous bed motion, and thus this feature could not be studied here. However, the mentioned homogenous sensitivity over almost the full AFOV renders this currently a mood point. Beyond that, it can be safely assumed that the current results were mostly unaffected by the axial phantom position, and only at the very edge of the AFOV different results must be expected. However, once MRD 322 and continuous bed motion become available with the Biograph Vision Quadra, a re-evaluation of EARL compliance will become necessary.

Figure 6 also reveals a strong recovery with values above 0.5 for RC_{max} and RC_{mean} in the smallest sphere. It can therefore be assumed that the Biograph Vision Quadra is able to resolve even smaller structures. Its combination of high spatial resolution and high imaging sensitivity might require the introduction of smaller phantom spheres to analyze imaging properties at scales smaller than 10 mm, especially with the anticipated future sensitivity gains. To cover these smaller scales, we are planning to introduce smaller hot phantom spheres without cold walls [41], using additive manufacturing [42]. Employing long-lived phantoms will also allow evaluating the entire AFOV with a constant count rate in one single session.

5. Conclusion

We conclude that EARL1 compliant reconstructions are possible with frames as short as 10 sec duration on the Biograph Vision Quadra, provided that the reconstruction parameters are carefully chosen. Optimal EARL1 compliant TrueX reconstruction for short frames were 6 iterations, 5 subsets and 7.8 mm Gauss filtering. To achieve the same short frames for EARL2 compliant measurements, it would be necessary to lower the EARL2 limits closer to unity.

While EARL 1 compliance proved very robust in terms of exposure, EARL2 compliance required a more careful selection of image reconstruction parameters. Especially, exposure was restricted to values between 0.6 MDecays/ml to 11.5 MDecays/ml. Optimal EARL2 compliant TrueX reconstructions were

achieved with 4 iterations, 5 subsets, and 4.6 mm Gauss FWHM post-reconstruction filtering. From the three analyzed recovery metrics, RC_{peak} was the most stable in respect to exposure, but using the suggested reconstruction parameters, RC_{max} and RC_{mean} become also useful quantitative metrics under varying exposure.

It came somewhat to a surprise, that EARL2 compliant exposure had an upper limit, meaning acquisition duration can actually become too long and with it the PET image becomes too noise-free. This certainly warrants a re-evaluation of EARL2 limits and possibly even the EARL procedures for total-body PET/CT systems: The lower achievable image noise justifies adjusting the bounds of the RC_{max} metric closer to unity. EARL guidelines with a more flexible acquisition duration can also be discussed, mainly formulated in terms of exposure. Harmonizing recovery values in respect to minimal or maximal attainable exposures would enhance comparability within frames of controlled dynamic studies and between dynamic studies across different PET/CT sites. This would make EARL, an already formidable harmonization strategy [26], even better.

Abbreviations

AFOV: Axial field of view; CT: Computed tomography; EANM: European Association of Nuclear Medicine; EARL: EANM Research Ltd; FOV: Field of view; LSO: Lutetium oxyorthosilicate; NEMA: National Electrical Manufacturers Association; nRMSE: normalized root mean square error; OSEM: Ordered subset expectation maximization; PET: positron emission tomography; PSF: Point spread function; PVE: partial volume effect; RC: Recovery coefficient; SNR: Signal to noise ratio; TOF: Time of flight; VOI: Volume of interest

6. Declarations

Funding

No funding was received.

Availability of data and materials

The datasets used and analyzed during the current study are available from the corresponding author on reasonable request.

Ethics approval and consent to participate

Not applicable.

Consent for publication

Not applicable.

Competing interests

Hasan Sari is a full-time employee of Siemens Healthcare AG, Switzerland. No other potential competing interest relevant to this article exist.

Authors' contributions

GAP and MH designed the study. GAP performed data collection and data analysis. HS performed data analysis. TW and GAP wrote the software for data analysis. AR coordinated the research. All authors discussed the results and implications and commented on the manuscript. All authors read and approved the final manuscript.

Acknowledgements

Thank goes to the IT-staff at the Department of Nuclear Medicine, Inselspital Bern, for assistance with the image reconstruction server.

Author's information

GAP is a member of the Swiss Working Group for clinical Cancer Research (Schweizerische Arbeitsgemeinschaft für Klinische Krebsforschung, SAKK).

7. References

1. Ter-Pogossian MM, Phelps ME, Hoffman EJ, Mullani NA. A Positron-Emission Transaxial Tomograph for Nuclear Imaging (PETT). Radiology. 1975;114:89-98. doi:10.1148/114.1.89.

2. Budinger TF. Time-of-Flight Positron Emission Tomography: Status Relative to Conventional PET. Journal of Nuclear Medicine. 1983;24:73-8.

3. Casey ME. Improving PET With HD•PET + Time of Flight. Siemens; 2008.

386 4. Martí-Climent JM, Prieto E, Domínguez-Prado I, García-Velloso MJ, Rodríguez-Fraile M, Arbizu J,
387 et al. Contribution of time of flight and point spread function modeling to the performance characteristics
388 of the PET/CT Biograph mCT scanner. Rev Esp Med Nucl Imagen Mol. 2013;32.

389 5. Alberts I, Prenosil G, Sachpekidis C, Weitzel T, Shi K, Rominger A, et al. Digital versus analogue
390 PET in [68Ga]Ga-PSMA-11 PET/CT for recurrent prostate cancer: a matched-pair comparison.
391 European Journal of Nuclear Medicine and Molecular Imaging. 2020;47:614-23. doi:10.1007/s00259-
392 019-04630-y.

393 6. Surti S, Viswanath V, Daube-Witherspoom ME, Conti M, Casey ME, Karp JS. Benefit of improved
394 performance with state-of-the art digital PET/CT for lesion detection in oncology. Journal of nuclear
395 medicine : official publication, Society of Nuclear Medicine. 2020. doi:10.2967/jnumed.120.242305.

396 7. van Sluis J, Boellaard R, Dierckx RAJO, Stormezand GN, Glaudemans AWJM, Noordzij W. Image
397 Quality and Activity Optimization in Oncologic 18F-FDG PET Using the Digital Biograph Vision PET/CT
398 System. Journal of Nuclear Medicine. 2020;61:764-71. doi:10.2967/jnumed.119.234351.

399 8. Rahmim A, Qi J, Sossi V. Resolution modeling in PET imaging: Theory, practice, benefits, and
400 pitfalls. Medical Physics. 2013;40:15. doi:10.1118/1.4800806.

401 9. Leahy R, Qi J. Statistical approaches in quantitative positron emission tomography. Statistics and
402 Computing. 2000;10:147-65.

403 10. Badawi RD, Shi H, Hu P, Chen S, Xu T, Price PM, et al. First Human Imaging Studies with the
404 EXPLORER Total-Body PET Scanner*. Journal of Nuclear Medicine. 2019;60:299-303.
405 doi:10.2967/jnumed.119.226498.

406 11. Siegel S, Aykac M, Bal H, Bendriem B, Bharkhada D, Cabello J, et al. Preliminary Performance of
407 a Prototype, One-Meter Long PET Tomograph. 2020 IEEE Nuclear Science Symposium & Medical
408 Imaging Conference. Virtual: IEEE; 2020.

409 12. van Sluis J, de Jong J, Schaar J, Noordzij W, van Snick P, Dierckx R, et al. Performance
410 Characteristics of the Digital Biograph Vision PET/CT System. Journal of Nuclear Medicine.
411 2019;60:1031-6. doi:10.2967/jnumed.118.215418.

412 13. Prenosil GA, Sari H, Fürstner M, Afshar-Oromieh A, Shi K, Rominger A, et al. Performance
413 Characteristics of the Biograph Vision Quadra PET/CT system with long axial field of view using the
414 NEMA NU 2-2018 Standard. Journal of Nuclear Medicine. 2021:jnumed.121.261972.
415 doi:10.2967/jnumed.121.261972.

416 14. Fahey FH, Kinahan PE, Doot RK, Kocak M, Thurston H, Poussaint TY. Variability in PET quantitation
417 within a multicenter consortium. Medical Physics. 2010;37:3660-6. doi:10.1118/1.3455705.

418 15. Lin C, Bradshaw T, Perk T, Harmon S, Eickhoff J, Jallow N, et al. Repeatability of Quantitative 18F-
419 NaF PET: A Multicenter Study. Journal of nuclear medicine : official publication, Society of Nuclear
420 Medicine. 2016;57:1872-9. doi:10.2967/jnumed.116.177295.

421 16. Armstrong IS, Kelly MD, Williams HA, Matthews JC. Impact of point spread function modelling and
422 time of flight on FDG uptake measurements in lung lesions using alternative filtering strategies. EJNMMI
423 Physics. 2014;1. doi:10.1186/s40658-014-0099-3.

424 17. National Electrical Manufacturers Association. NEMA Standards Publication NU 2-1994:
425 Performance Measurements of Positron Emission Tomographs. In: Association NEM, editor. 12 ed.
426 Washington DC: National Electrical Manufacturers Association; 1994.

427 18. National Electrical Manufacturers Association. NEMA Standards Publication NU 2-2018:
428 Performance Measurements of Positron Emission Tomographs (PET). In: Association NEM, editor. 18
429 ed. 1300 N. 17th Street, Suite 900, Rosslyn, VA 22209: National Electrical Manufacturers Association;
430 2018. p. 41.

19. Prenosil GA, Weitzel T, Hentschel M, Klaeser B, Krause T. Transconvolution and the virtual positron emission tomograph – A new method for cross calibration in quantitative PET/CT imaging. Medical Physics. 2013;40:15. doi:10.1118/1.4805112.

20. Prenosil GA, Klaeser B, Hentschel M, Fürstner M, Berndt M, Krause T, et al. Isotope independent determination of PET/CT modulation transfer functions from phantom measurements on spheres. Medical Physics. 2016;43:5767-78. doi:10.1118/1.4963217.

21. Prenosil GA, Hentschel M, Furstner M, Krause T, Weitzel T, Klaeser B. Technical Note: Transconvolution based equalization of positron energy effects for the use of 68 Ge/68 Ga phantoms in determining 18 F PET recovery. Medical physics. 2017;44:3761-6. doi:10.1002/mp.12330.

22. Quak E, Le Roux P-Y, Hofman M, Robin P, Bourhis D, Callahan J, et al. Harmonizing FDG PET quantification while maintaining optimal lesion detection: prospective multicentre validation in 517 oncology patients. European Journal of Nuclear Medicine and Molecular Imaging. 2015:1-11. doi:10.1007/s00259-015-3128-0.

23. Boellaard R, Oyen W, Hoekstra C, Hoekstra O, Visser E, Willemsen A, et al. The Netherlands protocol for standardisation and quantification of FDG whole body PET studies in multi-centre trials. European Journal of Nuclear Medicine and Molecular Imaging. 2008;35:2320-33. doi:10.1007/s00259-008-0874-2.

24. Boellaard R, Delgado-Bolton R, Oyen WJG, Giammarile F, Tatsch K, Eschner W, et al. FDG PET/CT: EANM procedure guidelines for tumour imaging: version 2.0. European Journal of Nuclear Medicine and Molecular Imaging. 2015;42:328-54. doi:10.1007/s00259-014-2961-x.

25. Aide N, Lasnon C, Veit-Haibach P, Sera T, Sattler B, Boellaard R. EANM/EARL harmonization strategies in PET quantification: from daily practice to multicentre oncological studies. European journal of nuclear medicine and molecular imaging. 2017;44:17-31. doi:10.1007/s00259-017-3740-2.

26. Koopman D, Jager PL, Slump CH, Knollema S, van Dalen JA. SUV variability in EARL-accredited conventional and digital PET. EJNMMI Research. 2019;9:106. doi:10.1186/s13550-019-0569-7.

27. Kaalep A, Sera T, Rijnsdorp S, Yaqub M, Talsma A, Lodge MA, et al. Feasibility of state of the art PET/CT systems performance harmonisation. European Journal of Nuclear Medicine and Molecular Imaging. 2018;45:1344-61. doi:10.1007/s00259-018-3977-4.

28. Pilz J, Hehenwarter L, Zimmermann G, Rendl G, Schweighofer-Zwink G, Beheshti M, et al. Feasibility of equivalent performance of 3D TOF [18F]-FDG PET/CT with reduced acquisition time using clinical and semiquantitative parameters. EJNMMI Research. 2021;11:44. doi:10.1186/s13550-021-00784-9.

29. Prenosil GA, Weitzel T, Fürstner M, Hentschel M, Krause T, Cumming P, et al. Towards guidelines to harmonize textural features in PET: Haralick textural features vary with image noise, but exposure-invariant domains enable comparable PET radiomics. PLOS ONE. 2020;15:e0229560. doi:10.1371/journal.pone.0229560.

30. Kaalep A, Burggraaff CN, Pieplenbosch S, Verwer EE, Sera T, Zijlstra J, et al. Quantitative implications of the updated EARL 2019 PET–CT performance standards. EJNMMI Physics. 2019;6:28. doi:10.1186/s40658-019-0257-8.

31. EARL. SUV recovery coefficients for ^{18}F standards 1 and 2. Schmalzhofgasse 26, 1060 Vienna, Austria: EANM Forschungs GmbH; 2020.

32. International Electrotechnical Commission. IEC Standard 61675-1: Radionuclide imaging devices - Characteristics and test conditions - Part 1: Positron emission tomographs Geneva, Switzerland: International Electrotechnical Commission 1998. p. 36.

33. Boellaard R, Krak NC, Hoekstra OS, Lammertsma AA. Effects of Noise, Image Resolution, and ROI Definition on the Accuracy of Standard Uptake Values: A Simulation Study. Journal of Nuclear Medicine. 2004;45:1519-27.

34. Krak NC, Boellaard R, Hoekstra OS, Twisk JWR, Hoekstra CJ, Lammertsma AA. Effects of ROI definition and reconstruction method on quantitative outcome and applicability in a response monitoring trial. European Journal of Nuclear Medicine and Molecular Imaging. 2005;32:294-301. doi:10.1007/s00259-004-1566-1.

35. Munk OL, Tolbod LP, Hansen SB, Bogsrud TV. Point-spread function reconstructed PET images of sub-centimeter lesions are not quantitative. EJNMMI Physics. 2017;4:5. doi:10.1186/s40658-016-0169-9.

36. Devriese J, Beels L, Maes A, Van de Wiele C, Pottel H. Impact of PET reconstruction protocols on quantification of lesions that fulfil the PERCIST lesion inclusion criteria. EJNMMI Physics. 2018;5:35. doi:10.1186/s40658-018-0235-6.

37. Nuyts J. Unconstrained image reconstruction with resolution modelling does not have a unique solution. EJNMMI Phys. 2014;1:98. doi:10.1186/s40658-014-0098-4.

38. Barrett HH, Wilson DW, Tsui BM. Noise properties of the EM algorithm: I. Theory. Physics in medicine and biology. 1994;39:833-46.

39. Wilson DW, Tsui BM, Barrett HH. Noise properties of the EM algorithm: II. Monte Carlo simulations. Physics in medicine and biology. 1994;39:847-71.

40. Teymurazyan A, Riauka T, Jans H-S, Robinson D. Properties of Noise in Positron Emission Tomography Images Reconstructed with Filtered-Backprojection and Row-Action Maximum Likelihood Algorithm. Journal of Digital Imaging. 2013;26:447-56. doi:10.1007/s10278-012-9511-5.

41. Hofheinz F, Dittrich S, Potzsch C, Hoff J. Effects of cold sphere walls in PET phantom measurements on the volume reproducing threshold. Physics in medicine and biology. 2010;55:1099-113. doi:10.1088/0031-9155/55/4/013.

42. Läppchen T, Meier LP, Fürstner M, Prenosil GA, Krause T, Rominger A, et al. 3D printing of radioactive phantoms for nuclear medicine imaging. European Journal of Nuclear Medicine and Molecular Imaging Physics. 2020;7:22. doi:10.1186/s40658-020-00292-0.